Ambiguity-Free 3D Millimeter-Precision RFID Tag Localization Inside Building Materials

Guoyi Xu
School of Electrical and Computer Engineering
Cornell University
Ithaca, NY, USA
https://orcid.org/0000-0002-8241-253X

Edwin C. Kan
School of Electrical and Computer Engineering
Cornell University
Ithaca, NY, USA
eck5@cornell.edu

Abstract— **Phase-based 3D radio-frequency identification (RFID) tag localization has the advantage of high accuracy, but the inherent phase-range ambiguity needs to be resolved by either frequency or spatial diversity. We propose a reliable 3D tag localization method that exploits spatial diversity to achieve millimeter-precision inside building materials with heavy multi-path interferences. We first obtain the functional relationship between differential phase and differential distance using polynomial fitting and optimization for reference tags and then evaluate the 3D positions of new tags given only phase measurements. A novel ambiguity-free algorithm is devised to identify the correct tag location from multiple candidates by leveraging redundant channel resources with spatial diversity. We prototyped the tag localization system on Universal Software Radio Peripheral (USRP) devices and harmonic backscatter RFID tags and demonstrated millimeter-level localization accuracy at 1.8 GHz second-harmonic carrier frequency inside building materials.**

Keywords—harmonic backscatter, phase ambiguity, phase measurements, precision localization, radio-frequency identification (RFID)

I. INTRODUCTION

Radio-frequency identification (RFID) has mature applications in highway tolling [1], luggage tracking [2], and supply chain management [3]. Recently, RFID tag localization has emerged as one of the critical applications for the Internet of Things (IoT) and structural integrity monitoring. For example, passive tags can be buried inside the weight bearing structures as markers to track displacement and vibration [4]. Moreover, the channel phase measurements can also be applied to sensing tasks such as localization and mapping [5], [6], imaging [7], [8], and detection of vital signs [9], [10]. Compared with received signal strength indicator (RSSI), the phase methods are often more sensitive to range, enabling accurate localization [11].

However, phase measurements suffer from ambiguity issues which result in large localization errors if not handled properly. They can be resolved by exploiting either frequency or spatial diversity. For example, frequency diversity can be exploited by calculating time-of-flight (ToF) or time-difference-of-arrival (TDoA) using wideband signals, as in traditional ToF radar systems [12]. In addition, a heuristic method [5] can remove phase ambiguity due to cyclic wavelength and optimize ranging accuracy by selecting a number of frequencies within a sparse bandwidth rather than occupying continuous frequency spectrums. Furthermore, by optimizing array placement and adopting array processing algorithms, spatial diversity is introduced and unambiguous angle-of-arrival (AoA) can be retrieved to improve localization [13]–[15]. Nonlinear and non-monotonic relationship between phase and range also causes location ambiguities, especially when the sensing devices are near the measured target under heavy multi-path [16]–[18]. Even if non-line-of-sight (NLoS) can be identified and filtered through AoA estimation [19], [20], near-field propagation exhibits nonlinear and non-monotonic phase-range relationship, degrading the localization accuracy of range-based approaches. Therefore, near-field localization methods are usually based on dedicated signal models and avoid range-based trilateration [16], [21].

In this paper, we propose a novel phase-based localization method that exploits spatial diversity to remove ambiguity from near-field nonlinearity. First, reference tag locations are selected, where differential phases for multiple receiver (Rx) pairs for a shared transmitter (Tx) are measured and calibrated. These relational functions with respect to differential distances from the tag to each pair of Rx antennas are then employed to determine differential distances given differential phases for an unknown tag location. Such functions can be nonlinear and non-monotonic due to near-field propagation and multi-path, producing multiple ambiguous distances for one differential phase and leading to ambiguous tag locations. An algorithm was devised to remove the nonlinearity ambiguity, where redundant channel resources from spatially diverse Rx antennas were exploited. We prototyped a millimeter-level 3D localization system by the harmonic backscatter RFID tag and universal software radio peripheral (USRP) devices. Ambiguity due to phase rotation over multiple wavelengths can be another concern, though with many available solutions in the literature [5], [22]. Due to length limitation and the present small-scale setup of the building-material prototype, complete integration with wavelength ambiguity resolution will be treated in the future for an extended large-scale setup.

II. PRECISION 3D TAG LOCALIZATION IN SMALL VOLUME

First, we introduce the complete 3D localization workflow which includes reference tag calibration and non-reference tag localization. Next, we describe the iterative polynomial fitting and optimization algorithm for the phase-distance function during reference tag calibration. Then, the voxel tree parsing algorithm is introduced for non-reference tag localization.

Finally, we propose the ambiguity-free tag localization algorithm, which exploits channel redundancy associated with spatially diverse Rx antennas.

A. 3D Localization Workflow

The workflow for tag 3D localization includes the reference tag calibration and non-reference tag localization, as shown in Figs. 1(a) and (b), respectively. Within the small capture volume, several tags were selected as reference locations, for which differential phases of backscattered signals were measured and calibrated. Differential phase varied with the corresponding differential distance from the tag to the two associated Rx antennas, and their functional relationship was obtained and improved through iterative polynomial fitting. This will be discussed in detail in Sec. II.B.
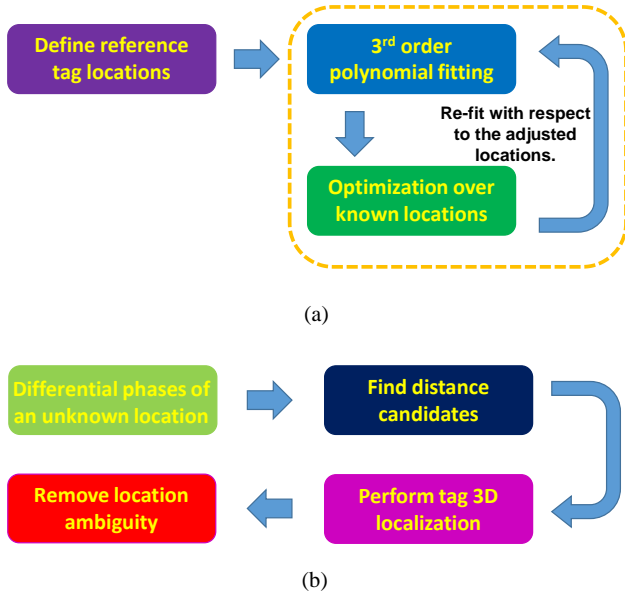

(a)

(b)

Fig. 1. Localization workflow. (a) Reference tag calibration. (b) Non-reference tag localization.

Then, for a non-reference tag with unknown location, the associated differential distances with given differential phases for each Rx pair can be extracted from the optimized polynomial functions in the previous calibration step. Combining the differential distances from multiple Rx pairs, we evaluated the 3D tag location by searching for the intersection point of multiple hyperboloid surfaces with the voxel tree parsing algorithm in Sec. II.C.

However, the optimized phase-distance functions can be nonlinear and non-monotonic, introducing multiple differential distance candidates for a single differential phase. As a result, there can be multiple ambiguous tag 3D locations. We removed such ambiguity by leveraging redundant channel resources from spatially diverse Rx antennas, as described in Sec. II.D.

B. Reference Tag Calibration

Suppose there were 1 Tx and M Rx antennas with known locations, and we selected N reference tag locations for which the differential phase for each Rx pair was measured. The differential phase and distance were employed to eliminate the dependence on absolute phase values which can be random for

different transceivers [23]. With the shared Tx, there were $M(M-1)/2$ different Rx pairs in total. The differential distance can be calculated as:

$$d_{n,k,l} = |\vec{r_n} - \vec{R_k}| - |\vec{r_n} - \vec{R_l}| \qquad (1)$$

where $\vec{r_n}$, $\vec{R_k}$ and $\vec{R_l}$ are the n-th reference tag location and locations of the k-th and l-th Rx antennas, respectively, for $1 \leq n \leq N$, and $1 \leq k \neq l \leq M$. For a given Rx pair, the 3$^{\text{rd}}$-order polynomial function that fitted the set of measured differential phases $\{\phi_{n,k,l}\}$ and the set of differential distances $\{d_{n,k,l}\}$ for the k-th and l-th Rx antenna pair can be expressed as:

$$\Phi_{k,l}(d_{k,l}) = p_{0,k,l}\left(\frac{d_{k,l} - \mu_{k,l}}{\sigma_{k,l}}\right)^3$$
$$+ p_{1,k,l}\left(\frac{d_{k,l} - \mu_{k,l}}{\sigma_{k,l}}\right)^2 + p_{2,k,l}\left(\frac{d_{k,l} - \mu_{k,l}}{\sigma_{k,l}}\right) + p_{3,k,l} \qquad (2)$$

where $d_{k,l}$ was the independent variable, and $p_{0,k,l}$, $p_{1,k,l}$, $p_{2,k,l}$ and $p_{3,k,l}$ were constant coefficients determined by the least-square polynomial fitting. For different Rx pairs we would get a different function $\Phi_{k,l}(d_{k,l})$ where $\mu_{k,l}$ and $\sigma_{k,l}$ were the mean and standard deviation of the set $\{d_{n,k,l}\}$ for given k and l. To avoid inverting an ill-conditioned Vandermonde matrix to get a more reliable fit, the samples $\{d_{n,k,l}\}$ are centered around their mean $\mu_{k,l}$ and normalized by their standard deviation $\sigma_{k,l}$ before the polynomial fitting procedure [24], [25].

The reference tags and Rx antenna locations were measured from the antenna physical centers, which might be inaccurate due to antenna detuning through mutual coupling. To further improve the polynomial fitting, optimization was performed with respect to the reference tag and Rx antenna locations. The objective function was defined as:

$$f(\vec{r_n}, \vec{R_k}, \vec{R_l}) = \sum_{k,l}\sum_n \left|\Phi_{k,l}(d_{n,k,l}) - \phi_{n,k,l}\right|^2$$
$$\underset{\vec{r_n}, \vec{R_k}, \vec{R_l}}{\operatorname{argmin}} f(\vec{r_n}, \vec{R_k}, \vec{R_l}) \qquad (3)$$

where $\Phi_{k,l}(d_{n,k,l})$ was the differential phase predicted by the polynomial function at $d_{n,k,l}$ using Eq. (2), and $\phi_{n,k,l}$ was the measured differential phase associated with the n-th reference tag location for the pair of the k-th and l-th Rx antennas. The objective function combined the phase prediction errors from all Rx-pair and reference tag locations, and the best locations of the reference tags and Rx antennas were determined by minimizing the objective function. Coefficients $p_{0,k,l}$, $p_{1,k,l}$, $p_{2,k,l}$ and $p_{3,k,l}$ for each Rx pair were constant during optimization by Eq. (3). We adopted the line search optimization for the objective function, and implemented the steepest descent algorithm with the strong Wolfe conditions [26]. Then, the updated locations $\vec{r_n}$, $\vec{R_k}$ and $\vec{R_l}$ were plugged back to Eq. (1) to calculate the updated differential distances. Polynomial fitting in Eq. (2) was performed again for the updated locations and iterated with optimization by Eq. (3). This iterative fitting and optimization routine gradually reduced the fitting errors by the polynomial functions $\Phi_{j,k}(d_{j,k})$ for all j and k.

The optimized polynomial functions would be employed to extract differential distances for non-reference 3D tag
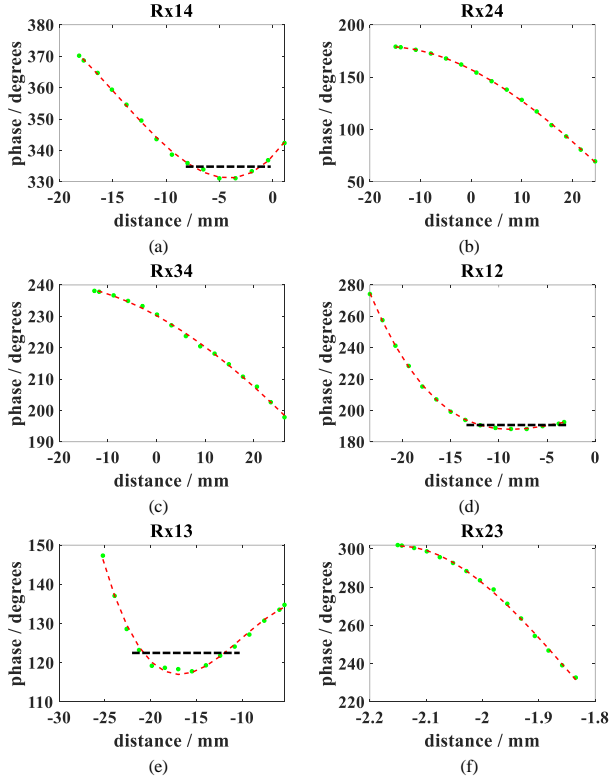
Fig. 2. (a-f) Polynomial curves for differential phases vs. differential distances after iterative fitting and optimization for each Rx pair.

localization. The optimized curves for 6 Rx pairs associated with 4 Rx antennas were shown in Fig. 2. It is observed that for Rx pairs in Figs. 2(a)(d)(e), curves were non-monotonic such that for certain differential phases, more than one differential distances can exist, as shown by the intersection with the black horizontal dashed lines. This produced ambiguous tag locations to be resolved by channel redundancy, as discussed in Sec. II.D.

C. Voxel Tree Parsing Algorithm

For each Rx pair, the tag location is on a hyperbolical surface which has constant differential distance from the foci, i.e., two Rx antennas. Fig. 3(b) shows the two-sheet hyperbolic surface, where a tag location resides on one sheet given the differential distance of an Rx pair. Thus, we need to know the intersection of hyperboloid surfaces associated with each Rx pair to identify the tag location. For this work, we selected 4 Rx pairs to obtain 1 tag location at the surface intersection. Fig. 3(a) shows the top-level flow chart for the voxel tree parsing algorithm that searches for the voxel corresponding to the tag location. The algorithm details are laid out in Algorithm I, as shown below. The exponential reduction in the oct-tree voxel can be readily integrated with the wavelength ambiguity resolution method if necessary.

Algorithm I

Initialize parameters:
- Differential distances: $d_{k,l}$ ($1 \leq k \neq l \leq M$).
- Rx antenna locations: $\overrightarrow{R_m}$ ($1 \leq m \leq M$) [1].

---
[1] For an Rx pair, we denoted "the k-th and l-th Rx antennas", with $1 \leq k \neq l \leq M$. Here, we denote Rx antennas individually, hence use the index m with
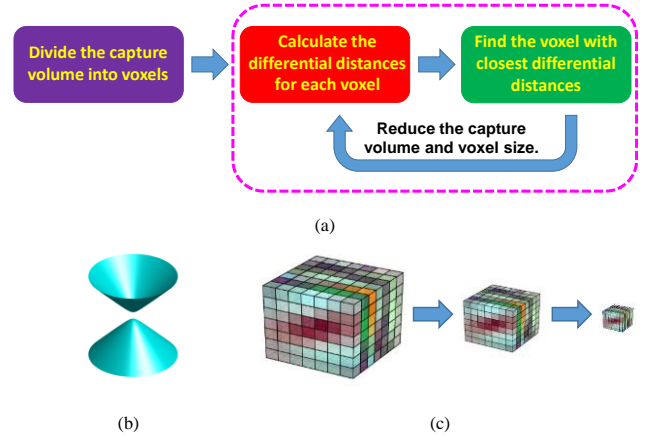

Fig. 3. (a) The voxel tree parsing algorithm. (b) A two-sheet hyperbolic surface. (c) Exponential reduction of the capture volume and voxel size in the voxel-tree parsing algorithm.

- Reference tag locations: $\overrightarrow{r_n}$ ($1 \leq n \leq N$).
- Capture volume: $X_{min}, X_{max}, Y_{min}, Y_{max}, Z_{min}, Z_{max}$.
- Number of voxels in each dimension: N_X, N_Y, N_Z.
- Capture colume reduction factor after each iteration: ρ_{CapVol}.

Define the capture volume and voxels:
- **Divide the capture volume** spanning $x \in [X_{min}, X_{max}]$, $y \in [Y_{min}, Y_{max}]$, and $z \in [Z_{min}, Z_{max}]$ equally into N_X, N_Y, and N_Z segments, respectively, thus totally $N_X \cdot N_Y \cdot N_Z$ voxels of equal sizes.
- **Record voxel locations** $\overrightarrow{a_p} = (x_p, y_p, z_p)$ ($1 \leq p \leq N_X \cdot N_Y \cdot N_Z$).
- **Calculate differential distances for each voxel and Rx pair**, i.e., $d(\overrightarrow{a_p}, \overrightarrow{R_k}, \overrightarrow{R_l}) = |\overrightarrow{a_p} - \overrightarrow{R_k}| - |\overrightarrow{a_p} - \overrightarrow{R_l}|$ ($1 \leq k \neq l \leq M$).

In $N_{MaxIter}$ iterations:
1) For each voxel, calculate $g(\overrightarrow{a_p}) = \sum_{k,l} |d(\overrightarrow{a_p}, \overrightarrow{R_k}, \overrightarrow{R_l}) - d_{k,l}|$. **Define $\widehat{\widehat{a}} = \underset{\overrightarrow{a_p}}{\operatorname{argmin}} \, g(\overrightarrow{a_p})$ as the tag location candidate**.
2) **Exit if this is the $N_{MaxIter}$ -th iteration, otherwise continue**.
3) **Define a new capture volume centered around $\widehat{\widehat{a}}$** with reduced volume size by ρ_{CapVol} in every dimension.
4) **Divide the new capture volume** into $N_X \cdot N_Y \cdot N_Z$ voxels of equal sizes, and **update voxel locations** $\overrightarrow{a_p} = (x_p, y_p, z_p)$.
5) **Calculate differential distances for each voxel and Rx pair**, i.e., $d(\overrightarrow{a_p}, \overrightarrow{R_k}, \overrightarrow{R_l}) = |\overrightarrow{a_p} - \overrightarrow{R_k}| - |\overrightarrow{a_p} - \overrightarrow{R_l}|$.

Output the tag location $\widehat{\widehat{a}}$.

Fig. 3(c) visualizes the exponential capture volume reduction of the voxel tree parsing algorithm, which refines the resolution during each iteration.

D. Ambiguity-Free Tag Localization

Notice that for $M = 4$ Rx antennas, there are $M(M-1)/2 = 6$ Rx pairs, and as M increases the number of Rx pairs increases quadratically. Thus, for $M \geq 4$, there are always redundant Rx pairs. We propose a novel ambiguity-free tag localization algorithm which leverages redundant channels to remove tag

---
$1 \leq m \leq M$, and the m-th Rx antenna's location is denoted by $\overrightarrow{R_m}$. Otherwise, there is no difference in the sense that k, l, and m all represent antenna indices.
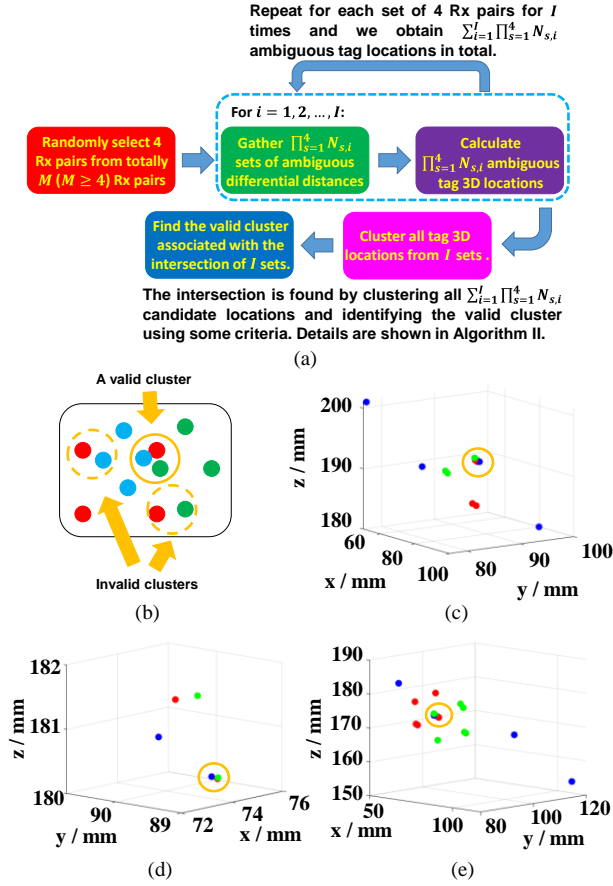
Fig. 4. (a) The ambiguity-free tag localization algorithm. (b) Visualization of Algorithm II. (c-e) 3 experimental examples of valid clusters corresponding to the intersection of sets of tag locations from different subsets of Rx pairs.

location ambiguity due to the non-monotonic polynomial functions. Taking $M = 4$ as an example, we have $\binom{6}{4} = 15$ different selections of 4 out of 6 Rx pairs. For each selection, suppose the s-th Rx pair produces N_s ambiguous differential distances, so there are $\prod_{s=1}^{4} N_s$ combinations of 4 differential distances in total, hence $\prod_{s=1}^{4} N_s$ ambiguous tag locations. Each selection of 4 Rx pairs produces a different set of ambiguous tag locations, and if Rx antennas are deployed with spatial diversity, the true tag location corresponds to the intersection of sets of tag locations produced by all selections of 4 Rx pairs. Fig. 4(a) shows the top-level flow chart for the ambiguity-free tag localization algorithm. Fig. 4(b) visualizes the intersection of tag location sets, with dots of the same color representing tag locations from the same selection of 4 Rx pairs. The algorithm is described in detail as shown in Algorithm II below.

Algorithm II

Initialize parameters:
- Number of different selections of 4 Rx pairs: I. ($I \leq \binom{M(M-1)/2}{4}$)
- The neighborhood search radius for clustering: ε.
- Minimum number of points to form a cluster: N_{minpts}.

For the i-th iteration ($1 \leq i \leq I$):
1) **Pick 1 set of 4 Rx pairs** that has not been selected in previous iterations.
2) For the s-th Rx pair with $1 \leq s \leq 4$, **obtain $N_{s,i}$ ambiguous differential distances**.[2]
3) **List all $J_i = \prod_{s=1}^{4} N_{s,i}$ combinations** of 4 differential distances from the 4 Rx pairs.
4) **Apply Algorithm I to each combination in 3)** to get the set of J_i ambiguous tag locations, i.e., $\{\vec{a}_j\}_i$. ($1 \leq j \leq J_i$)

Cluster all tag locations from sets $\{\vec{a}_j\}_i$.

Find the cluster that contains one tag location from each set $\{\vec{a}_j\}_i$ for $1 \leq i \leq I$, and output the geometric center of this cluster.

In this work, we heuristically selected $I = 3$. Due to phase noises, the correct tag location candidates from each selection of Rx pairs were not at the exact same location, but instead were close to each other. Thus, Algorithm II found such an "intersection" by spatial clustering. The density-based spatial clustering of applications with noise (DBSCAN) algorithm was adopted [27], for which the parameters of the search radius ε and the minimal number of points to form a cluster N_{minpts} were initialized at the beginning. Figs. 4(c-e) provides 3 examples of spatial clustering of tag location sets, each with $I = 3$ sets of
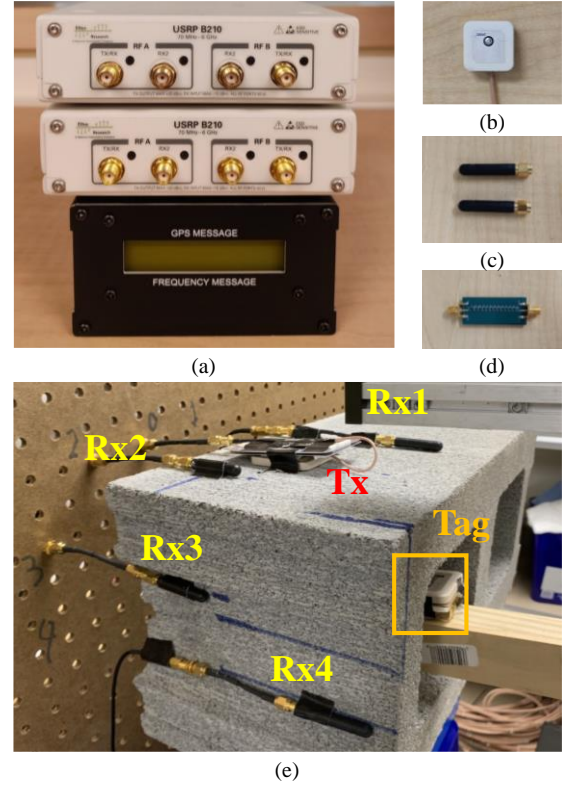

Fig. 5. Universal software radio peripheral (USRP) B210 devices and global positioning system disciplined oscillator (GPSDO). (b) A patch antenna operating around 900 MHz. (c) A whip antenna in the 1.8 GHz band. (d) A harmonic RFID tag. (e) The wireless setup for tag localization that consists of 1 Tx antenna and 4 Rx antennas, in a heavy multi-path channel by a concrete brick.

---

[2] With ambiguity due to non-monotonic phase-distance function, some Rx pairs will give $N_{s,i} > 1$. If $N_{s,i} = 1$ for all s and i, the ambiguity-free tag localization algorithm is no longer needed. In this case, Algorithm II degenerates into Algorithm I with proper modifications.

ambiguous tag locations from 4 Rx pairs, represented in red, blue and green dots, respectively. A valid cluster that corresponds to the true tag location is one that incorporates one dot of each color, marked out by yellow circles. Closely spaced tag locations in the yellow circles proves the effectiveness of the proposed ambiguity-free algorithm. When there are only 4 Rx pairs, ambiguity cannot be removed without prior knowledge, indicated by dots of the same color in Figs. 4(c-e). Therefore, spatial diversity is a critical prerequisite to remove ambiguity with confidence.

III. EXPERIMENTAL VALIDATION

A. Experimental Setup

We established an experimental setup for tag localization. Two National Instruments (NI) USRP Ettus B210 (Ettus Research, Austin, TX) devices were used, and synchronized with a global positioning system disciplined oscillator (GPSDO), as shown in Fig. 5(a). A patch antenna (Taoglas ISPC.91A with around 5 dBi gain at 900 MHz) was used as the Tx antenna as shown in Fig. 5(b). Four whip antennas (Siretta Delta 14 with around 1 dBi gain at 1.8 GHz) in Fig. 5(c) were used as Rx antennas. A harmonic backscattering RFID tag in Fig. 5(d) was used for localization [28]. Tag localization was performed in a heavy multi-path channel of 1 Tx antenna and 4 Rx antennas, implemented by a concrete brick to represent building materials, as shown in Fig. 5(e). During experiments, the tag was carried by a stepping motor with 1.25 µm stepping precision, and the linear trail was adjusted in both horizontal displacement and tilt orientation to test various spatially diverse tag 3D locations, as shown in Fig. 6(a).

B. Localization and Phase Noises

For each linear trip of the stepping motor, the motor stopped at 0.5 mm intervals to collect differential phase measurements, over a 40 mm trail. Multiple trips were taken with different horizontal and tilt orientations of the stepping motor, and around 5% of tag locations were selected as reference locations. We performed reference tag calibration and non-reference tag localization as introduced in Sec. II. In Fig. 6(b) the scatter plot included the ground truth locations by the stepping motor and the calculated tag locations by the localization algorithm, for both reference and non-reference tags, over 3 stepping motor trips with tilt angles of 0°, 1.3° and 2.7°, respectively. As expected, yellow and green dots matched well as they correspond to the reference tag locations. Red and blue dots represented the ground truth locations and calculated locations for non-reference tags, respectively. The cumulative distribution function (CDF) of the localization error over all 3 trips in Fig. 6(b) was shown in Fig. 6(c), which verified the millimeter-level accuracy.

To study the phase noise distributions, we calculated the empirical probability distribution functions (PDF) of the differential phases of various Rx pairs, using a Gaussian smoothing kernel [29]. Fig. 7 shows the examples of four Rx pairs. The location of Rx antennas will affect the phase variance due to signal propagation losses in the wireless channel, but for all measured channels, the empirical PDFs are nearly Gaussian. This justifies the use of the sample mean values to represent differential phases for each Rx pair during least-square fitting
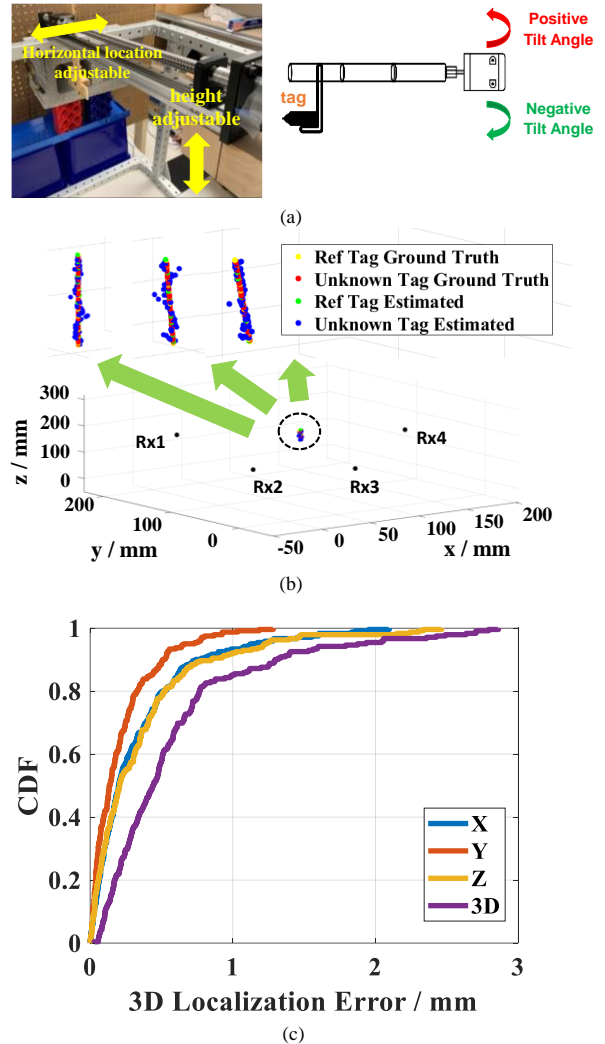

(a)

(b)

(c)

Fig. 6. (a) The stepping motor carrying the harmonic tag during experiments, whose horizontal displacement and tilt orientation were adjusted for multiple experiments. (b) The scatter plot of Rx antenna locations, together with ground truth locations and calculated tag locations for both reference and non-rerference tags, for three 40-mm stepping motor trips with 0.5 mm steps. (c) The cumulative distribution function (CDF) of localization errors for non-reference tag locations of all three stepping motor trips in (b).

and optimization in Eqs. (2) and (3). When no further information about the distribution can be implied, Gaussian distribution has the maximum entropy among all distributions with the same variance [30].

IV. CONCLUSION

In this paper, we propose a novel phase-based tag localization algorithm that removes ambiguity due to nonlinear and non-monotonic phase-distance functions in the near field, which leverages channel redundancy in spatially diverse Rx antennas. The iterative fitting and optimization algorithm for reference tag calibration and the voxel tree parsing algorithm for non-reference tag localization are introduced. Millimeter-level 3D localization accuracy was achieved in a setup of 1 Tx and 4 Rx. For future work, the current setup can be extended for multiple Tx and Rx antennas, by using multiplexing techniques
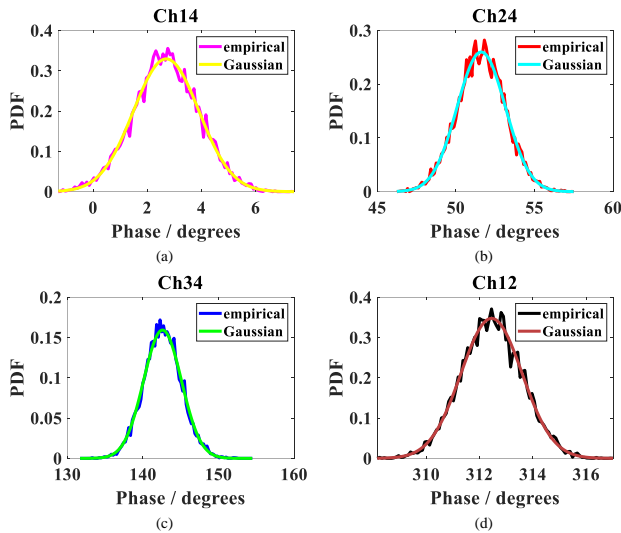
Fig. 7. (a-d) The empirical probability distribution functions (PDF) of differential phase measurements from four Rx pairs, and the correspoding Gaussian distributions with the same means and variances.

like frequency-division multiple access (FDMA) or code-division multiple access (CDMA) over multiple Tx.

REFERENCES

[1] B. Eckfeldt, "What does RFID do for the consumer?", *Communications of the ACM*, vol. 48, no. 9, pp. 77-79, Sep. 2005, doi: 10.1145/1081992.1082024.

[2] *Resolution: RFID Baggage Tracking Set for Global Deployment, IATA Pressroom,* IATA, Montreal, QC, Canada, Jun. 2019.

[3] Y.-M. Wang, Y.-S. Wang, and Y.-F. Yang, "Understanding the determinants of RFID adoption in the manufacturing industry," *Technol. Forecast. Soc. Change,* vol. 77, no. 5, pp. 803–815, Jun. 2010, doi: 10.1016/j.techfore.2010.03.006.

[4] J. Zhang, G. Y. Tian, A. M. J. Marindra, A. I. Sunny, and A. B. Zhao, "A review of passive RFID tag antenna-based sensors and systems for structural health monitoring applications," Sensors, vol. 17, no. 2, pp. 1-33, Feb. 2017, doi: 10.3390/s17020265.

[5] Y. Ma and E. C. Kan, "Accurate indoor ranging by broadband harmonic generation in passive NLTL backscatter tags," *IEEE Trans. Microw. Theory Tech.,* vol. 62, no. 5, pp. 1249–1261, May 2014, doi: 10.1109/TMTT.2014.2311381.

[6] E. D. Giampaolo, F. Martinelli, and F. Romanelli, "Robust simultaneous localization and mapping using the relative pose estimation of trilateration UHF RFID tags," *IEEE J. Radio Freq. Identif.,* vol. 6, pp. 583–592, 2022, doi: 10.1109/JRFID.2022.3179045.

[7] J. Wang, J. Xiong, X. Chen, H. Jiang, R. K. Balan, and D. Fang, "TagScan: simultaneous target imaging and material identification with commodity RFID devices," *Proc. the 23rd Annual Intl. Conf. Mobile Computing and Networking (MobiCom),* New York, NY, USA, Oct. 2017, doi: 10.1145/3117811.3117830.

[8] G. Xu, P. Sharma, X. Hui, and E. C. Kan, "3D indoor device-free object detection by passive radio-frequency identification," *IEEE Trans. Instrum. Meas.,* vol. 70, pp. 1–13, Feb. 2021, doi: 10.1109/TIM.2021.3059309.

[9] C. Yang, X. Wang, and S. Mao, "Respiration monitoring with RFID in driving environments," *IEEE J. Sel. Areas Commun.,* vol. 39, no. 2, pp. 500–512, Feb. 2021, doi: 10.1109/JSAC.2020.3020606.

[10] P. Sharma and E. C. Kan, "Sleep scoring with a UHF RFID tag by near field coherent sensing," *2018 IEEE/MTT-S Intl. Microwave Symposium (IMS),* Philadelphia, PA, USA, Jun. 2018, doi: 10.1109/MWSYM.2018.8439216.

[11] C. Li, L. Mo, and D. Zhang, "Review on UHF RFID localization methods," *IEEE J. Radio Freq. Identif.,* vol. 3, no. 4, pp. 205–215, Dec. 2019, doi: 10.1109/JRFID.2019.2924346.

[12] G. Piccinni, G. Avitabile, G. Coviello, and C. Talarico, "Real-time distance evaluation system for wireless localization," *IEEE Trans. Circuits Syst. Regul. Pap.,* vol. 67, no. 10, pp. 3320–3330, Oct. 2020, doi: 10.1109/TCSI.2020.2979347.

[13] R. Schmidt, "Multiple emitter location and signal parameter estimation," *IEEE Trans. Antennas Propag.,* vol. 34, no. 3, pp. 276–280, Mar. 1986, doi: 10.1109/TAP.1986.1143830.

[14] R. Roy and T. Kailath, "ESPRIT-estimation of signal parameters via rotational invariance techniques", *IEEE Trans. Acoust. Speech Signal Process.,* vol. 37, no. 7, pp. 984-995, July 1989, doi: 10.1109/29.32276.

[15] Y. Ma and E. C. Kan, "Passive ranging by low-directivity antennas with quality estimate," *2015 IEEE MTT-S Intl. Microwave Symposium,* Phoenix, AZ, USA, May 2015, doi: 10.1109/MWSYM.2015.7166879.

[16] B. Friedlander, "Localization of signals in the near-field of an antenna array," *IEEE Trans. Signal Process.,* vol. 67, no. 15, pp. 3885–3893, Aug. 2019, doi: 10.1109/TSP.2019.2923164.

[17] H. G. Schantz, "A real-time location system using near-field electromagnetic ranging," *2007 IEEE Antennas and Propagation Society International Symposium,* Honolulu, HI, USA, Jun. 2007, doi: 10.1109/APS.2007.4396365.

[18] E. Joy and D. Paris, "Spatial sampling and filtering in near-field measurements," *IEEE Trans. Antennas Propag.,* vol. 20, no. 3, pp. 253–261, May 1972, doi: 10.1109/TAP.1972.1140193.

[19] C. Wu, Z. Yang, Z. Zhou, K. Qian, Y. Liu, and M. Liu, "PhaseU: real-time LOS identification with WiFi," *2015 IEEE Conf. Computer Communications (INFOCOM),* Hong Kong, China, Apr. 2015, doi: 10.1109/INFOCOM.2015.7218588.

[20] J. Xiong and K. Jamieson, "ArrayTrack: a fine-grained indoor location system," *Proc. the 10th USENIX Conf. Networked Systems Design and Implementation,* Lombard, IL, USA, Apr. 2013, doi: doi/10.5555/2482626.2482635.

[21] D. Dardari, N. Decarli, A. Guerra, and F. Guidi, "LOS/NLOS near-field localization with a large reconfigurable intelligent surface," *IEEE Trans. Wirel. Commun.,* vol. 21, no. 6, pp. 4282–4294, Jun. 2022, doi: 10.1109/TWC.2021.3128415.

[22] L. Shangguan, Z. Yang, A. X. Liu, Z. Zhou, and Y. Liu, "STPP: spatial-temporal phase profiling-based method for relative RFID tag localization," *IEEE/ACM Trans. Netw.,* vol. 25, no. 1, pp. 596–609, Feb. 2017, doi: 10.1109/TNET.2016.2590996.

[23] T. Harzheim and H. Heuermann, "Phase repeatable synthesizers as a new harmonic phase standard for nonlinear network analysis," *IEEE Trans. Microw. Theory Tech.,* vol. 66, no. 6, pp. 2888–2895, Jun. 2018, doi: 10.1109/TMTT.2018.2817513.

[24] *Polynomial curve fitting - MATLAB polyfit.* Available: https://www.mathworks.com/help/matlab/ref/polyfit.html (accessed Feb. 21, 2023).

[25] W. Gautschi, "Optimally scaled and optimally conditioned Vandermonde and Vandermonde-like matrices," *BIT Numer. Math.,* vol. 51, no. 1, pp. 103–125, Mar. 2011, doi: 10.1007/s10543-010-0293-1.

[26] J. Nocedal and S. J. Wright, Eds., "Line search methods," in *Numerical Optimization, 2nd ed.,* New York, NY, USA: Springer, 2006, pp. 30–65.

[27] M. Ester, H.-P. Kriegel, J. Sander, and X. Xu, "A density-based algorithm for discovering clusters in large spatial databases with noise," *Proc. the Second Intl. Conf. Knowledge Discovery and Data Mining,* Portland, OR, USA, Aug. 1996, doi: 10.5555/3001460.3001507.

[28] F. Yu, K. G. Lyon, and E. C. Kan, "A novel passive RFID transponder using harmonic generation of nonlinear transmission lines," *IEEE Trans. Microw. Theory Tech.,* vol. 58, no. 12, pp. 4121–4127, Dec. 2010, doi: 10.1109/TMTT.2010.2088134.

[29] A. W, Bowman, and A. Azzalini, *Applied Smoothing Techniques for Data Analysis: The Kernel Approach with S-Plus Illustrations,* Oxford, UK: Oxford University Press, 1997.

[30] D. Dowson and A. Wragg, "Maximum-entropy distributions having prescribed first and second moments (Corresp.)," *IEEE Trans. Inf. Theory,* vol. 19, no. 5, pp. 689–693, Sep. 1973, doi: 10.1109/TIT.1973.1055060.